

The Relationship between Accretion and Ionised Ejection among Young Stellar Objects in the Coronet Cluster

Arpan Ghosh¹*, Roberto Galván-Madrid¹, Johan Ramírez-Arellano¹, Carlos Carrasco-González¹, Gráinne Costigan², Suzanne Ramsay³, Carlo Manara³, Jan Forbrich⁴, Hauyu Baobab Liu^{5,6}, Michihiro Takami⁷

¹Universidad Nacional Autónoma de México, Instituto de Radioastronomía y Astrofísica, 58090 Morelia, Michoacán, México

²Grünenthal GmbH

³European Southern Observatory, Karl-Schwarzschild-Strasse 2, 85748 Garching bei München, Germany

⁴Centre for Astrophysics Research, University of Hertfordshire, College Lane, Hatfield AL10 9AB, UK

⁵Department of Physics, National Sun Yat-Sen University, No. 70, Lien-Hai Road, Kaohsiung City 80424, Taiwan, R.O.C.

⁶Center of Astronomy and Gravitation, National Taiwan Normal University, Taipei 116, Taiwan, R.O.C.

⁷Institute of Astronomy and Astrophysics, Academia Sinica, 11F Astronomy-Mathematics Building, No.1, Sec. 4, Roosevelt Rd, Taipei 10617, Taiwan, R.O.C.

Accepted XXX. Received YYY; in original form ZZZ

ABSTRACT

We present results from a coordinated, multi-epoch near-infrared and centimeter radio survey of young stellar objects (YSOs) in the Coronet, aimed at probing the connection between mass accretion and ionised mass loss. Using VLT-KMOS, we detect Brγ emission in 5 of the 26 targets, which also exhibit 3.3-cm continuum emission in VLA images, consistent with partially ionised jets. For seven additional sources, stringent flux upper limits were obtained. The derived accretion and ionised mass-loss rates for class I and class II YSOs follow a sublinear correlation $\dot{M}_{\text{ion}} \propto \dot{M}_{\text{acc}}^{0.3}$, consistent with previous results for class II YSOs but extended here to earlier stages. Multi-epoch observations reveal modest variability in both tracers but no clear temporal correlation between accretion and ejection within timescales of a few months. The ratio $\dot{M}_{\text{ion}}/\dot{M}_{\text{acc}}$ shows an anti-correlation with \dot{M}_{acc} , increasing with time from class I YSOs to class II YSOs, suggesting an increase in jet-launching efficiency or ionisation fraction with evolution. These findings support a direct connection between accretion and outflow across the \sim Myr timescale of YSO evolution, while highlighting the complexity of their short-term interplay.

Key words: circumstellar matter – stars : activity — stars : evolution — stars : formation – stars : magnetic field

1 INTRODUCTION

The mass assembly during star formation occurs through the accretion of material from a circumstellar disk to the central object (Hartmann et al. 2016). During the earliest class 0 and I stages of Young Stellar Object evolution (YSO, Adams et al. 1987; Andre et al. 1993), the protostars and their disks are also surrounded by dense envelopes, which are cleared out within a Myr (Dunham et al. 2014). The later YSO stages (class II and III) are marked by the evolution of their disks, with a gradual decline in their gas content and accretion rates over a few Myr (Armitage et al. 2003; Williams & Cieza 2011; Manara et al. 2023; Gaidos et al. 2025).

A fraction of the accreted material is ejected in the form of jets and disk-winds, which are crucial for the release of specific angular momentum, as well as for disk dispersal (Frank et al. 2014; Pasucci et al. 2023). In standard theoretical models, the ejection and accretion of material are coupled through magnetohydrodynamical (MHD) processes (Shu et al. 1994; Pudritz et al. 2007). Therefore, a common expectation is that accretion and ejection will be coupled

in time. However, detailed theoretical modelling of these processes across YSO evolution is challenging (e.g., Romanova et al. 2018; Zhu 2025). Furthermore, YSOs show evidence of time variability within timescales much shorter than their evolutionary timescale in their accretion rates, ejected jets, and circumstellar material (e.g., Morales-Calderón et al. 2011; Fischer et al. 2023; Lora et al. 2024).

A joint characterisation of accretion and ejection processes across YSO evolutionary types requires multiwavelength data. Emission of hydrogen (H_I) recombination lines such as Brγ, emitted in the accretion shock around the stellar surface, have become the standard to measure accretion (Folha & Emerson 2001; Muzerolle et al. 2001). In the least embedded YSOs, jets and disk-winds are commonly studied via optical lines, e.g., [O_I] (Hartigan et al. 1995; Fang et al. 2018; Nisini et al. 2018; Banzatti et al. 2019), as well as with near-infrared molecular hydrogen H₂ emission (Takami et al. 2006; Contreras Peña et al. 2017; Guo et al. 2020). Radio continuum emission at centimeter wavelengths is known to be an effective tracer of the partially ionised base of jets (Rodríguez et al. 2014; Anglada et al. 2018). This tracer is particularly valuable in the more embedded class 0/I YSOs (Tychoniec et al. 2018). However, other physical processes can contribute to the observed centimetre emission. Non-thermal (gyro)synchrotron

* E-mail: a.ghosh@irya.unam.mx; 19aghosh91@gmail.com

emission from an active stellar magnetosphere is expected to dominate in class IIIIs and could contaminate the emission of less evolved YSOs (e.g., [Liu et al. 2014](#); [Forbrich et al. 2021](#)).

In this paper, we report the results of a coordinated monitoring of YSOs in the R Corona Australis (R CrA) star forming region, using Bry and centimeter continuum as tracers of accretion and ejection, respectively. Recent studies by [Rota et al. \(2025\)](#); [Garufi et al. \(2025\)](#); [Rota et al. \(2024\)](#) have explored the relationship between accretion and ejection using these tracers, but they have focused on class II YSOs, and their observations were not quasi-simultaneous. The *Coronet* cluster in R CrA is an excellent target because it is nearby (152 pc; [Galli et al. 2020](#), see also [Dzib et al. 2018](#)) and remains embedded in its natal cloud ([Sicilia-Aguilar et al. 2011](#)), hosting a large concentration of YSOs at different evolutionary stages ([Nisini et al. 2005a](#); [Sicilia-Aguilar et al. 2008](#); [Myers 2009](#); [Peterson et al. 2011](#); [Cazzoletti et al. 2019](#)). The Coronet has also been studied in the radio continuum ([Miettinen et al. 2008](#); [Choi et al. 2008](#); [Liu et al. 2014](#)), including monitoring campaigns with X-ray observations ([Forbrich et al. 2007](#)).

The paper is arranged as follows. Section 2 describes the observations and data analysis, followed by the results in Section 3. The implications of our results are discussed in Section 4, and Section 5 presents our conclusions.

2 OBSERVATIONS AND DATA ANALYSIS

2.1 Near-infrared data

We have selected a sample of 26 YSOs within the Coronet cluster, spanning the evolutionary range from class I to class III. The YSOs were selected from those reported by [Peterson et al. \(2011\)](#) in their study using *Spitzer*. The selected YSOs were observed with the K-band Multi Object Spectrograph (KMOS, [Sharples et al. 2013](#)) on the Very Large Telescope (VLT), using the K-band setup, which provides a wavelength coverage between 1.934 and 2.460 μm at a resolution of $R \sim 4200$. The observations were carried out between April 27 and July 22, 2014, as part of proposal ID 093.C-0657 (P.I. Galván-Madrid). The target-of-opportunity (ToO) mode was used, triggered by observations taken with the Very Large Array. The data were reduced using the KMOS version 2.7.3 pipeline within ESOREflex ([Davies et al. 2013](#); [Freudling et al. 2013](#)). The 1D spectrum was extracted by averaging over a 10×10 pixel region of the spatial axes centred on the source peak, chosen to maximize the S/N and ensure uniform aperture losses across epochs with varying seeing conditions. For epochs where the source was not well centred within the IFU field of view, a smaller region was adopted. The spatially integrated spectra from the output KMOS datacubes were calibrated using photometry obtained from the 2MASS ([Skrutskie et al. 2006](#)) and VISIONS ([Meingast et al. 2023](#)) surveys. In a way similar to [Fiorellino et al. \(2021\)](#), this latter procedure was adopted to improve the spectro-photometry of the original KMOS data.

2.2 Radio Data

Observations were conducted with the NRAO’s Karl G. Jansky Very Large Array (VLA). Partial results of the monitoring program, which ran from 2012 to 2015, have been published in [Liu et al. \(2014\)](#) and [Galván-Madrid et al. \(2014\)](#). The full results will be presented in Ramírez-Arellano et al. (in prep.). During the months of the KMOS program, the VLA observed for ten epochs: seven in the X band (3.3 cm) and three in the Ku band (2.1 cm). In this paper, we make use

Table 1. Summary of the parameters of the Bry detected sources. Sources with upper limits in both Bry and 3.3 cm are labelled ‘UL’.

Source	RA (J2000)	DEC (J2000)	YSO Class	Bry	3.3cm		Mass (M_{\odot})	Radius (R_{\odot})	A_V (mag)
					Radio	Mass			
IRS1	19:01:50.705	-36:58:09.55	I	Em	Yes	0.40	6.00	30.0	
IRS2	19:01:41.582	-36:58:31.07	I	Em	Yes	1.40	2.90	20.0	
CrA43	19:01:58.564	-36:57:08.23	I	Em	Yes	3.54	2.32	16.5	
IRS6	19:01:50.480	-36:56:37.90	II	Abs	Yes	0.20	2.32	29.0	
TCrA	19:01:58.784	-36:57:49.78	II	Em	Yes	2.25	1.14	2.5	
CrA16	19:01:33.877	-36:57:44.71	II	Em	Yes	0.32	1.22	16.6	
JVLA1	19:01:34.917	-37:00:56.84	III	Abs	Yes	1.34	1.94	1.4	
CrA26	19:02:06.833	-36:58:41.43	II	UL	UL	0.18	2.10	1.2	
Peterson1	19:01:32.345	-36:58:02.97	II	UL	UL	0.28	1.21	14.7	
Peterson6	19:01:53.775	-37:00:33.80	II	UL	UL	0.10	0.47	0.2	
IRS10	19:02:04.109	-36:57:00.72	II	UL	UL	0.16	1.68	9.76	

Notes. Stellar parameters are from [Nisini et al. \(2005b\)](#) and [Dong et al. \(2018\)](#). For CrA43, Peterson1, Peterson6, IRS10 and CrA26, parameters were obtained from SED fitting using SEDFITTER ([Robitaille et al. 2007](#)).

of the higher quality X-band data from those epochs, as well as the image created by concatenating the visibilities of 32 X-band epochs from the entire program.

The VLA observations were carried out in single-pointing mode, centered at $\alpha(\text{J2000}) = 19^h 01^m 48.0^s$, $\delta(\text{J2000}) = -36^{\circ} 57' 59.00''$. Data were calibrated using the Common Astronomy Software Applications package, version 6.5.4 ([CASA Team et al. 2022](#)). Standard calibration and imaging steps were followed (see [Liu et al. 2014](#)). The phases of the visibilities in each epoch were self-calibrated, and individual-epoch images were created with these. Also, deep images were made from the concatenated visibilities of all epochs. All the images used in this paper were produced using the `tclean` task within CASA, utilizing *Briggs* weighting with `robust = 0`. The central frequency of the images is 9.0 GHz (3.3 cm).

The most sensitive image is the one created with the concatenated visibilities. The rms noise prior to the correction of the primary-beam response is $9 \mu\text{Jy beam}^{-1}$. The FWHM beamsize of this image is $\theta_{maj} \times \theta_{min} = 1''.85 \times 0''.78$, with a position angle (P.A.) = 4.2° .

2.3 Flux measurements

We inspected the flux-calibrated, spatially averaged KMOS spectra of each epoch, looking for the Bry line at 2.166 μm . We detected Bry in seven out of the 26 targeted YSOs. Among them, the line was found to be in emission in five YSOs and in absorption in the remaining two (see Table 1). To measure the Bry fluxes, we fitted a model that includes a Gaussian for the Bry line and a first-order polynomial for the adjacent continuum. For this, we used the `LevMarLSQFitter` within the `astropy` modeling package ([Astropy Collaboration et al. 2022](#)). The line flux was measured as the area under the fitted Gaussian, along with the corresponding error propagation. This procedure was performed for the individual epochs and for the median-combined spectrum of each source. Of the remaining 19 targets, two (JVLA4 and Peterson4) had no detectable continuum within the IFU field of view, one (CrA19) had a coordinate mismatch with the radio data, and two with extended radio emission (IRS7E and IRS7W) were excluded. The remaining 14 sources show no Bry detection. These comprise seven class III, six class II, and one class I YSOs. The 1D spectra of the seven class II and class I sources from individual epochs were averaged and combined to produce a single spectrum. The upper limit on their Bry

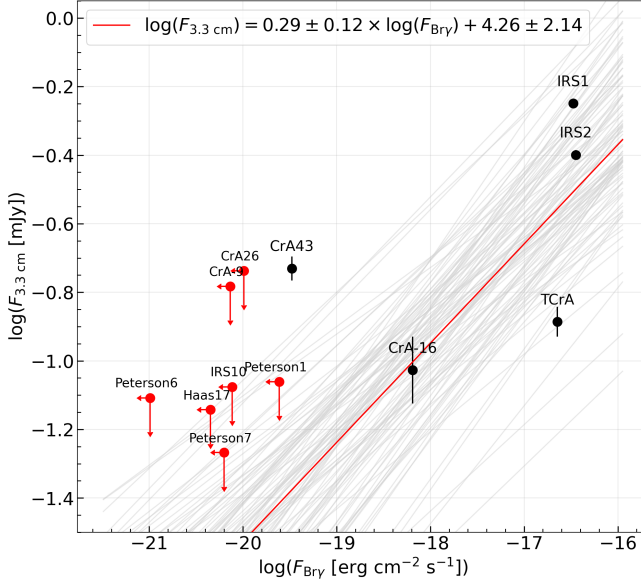


Figure 1. Relationship between the Bry and the 3.3 cm radio continuum fluxes for the class I and II sources. Detected sources are denoted by black symbols and upper limits by red symbols. Grey curves illustrate posterior regression lines consistent with the 68% credible interval of the slope; the median relation is shown in red.

flux was then estimated following the procedure of [Fiorellino et al. \(2021\)](#), modified as follows:

$$F_{\text{upper}} = 3 \times \sigma_{\text{rms}} \times \sqrt{N_{\text{chan}}} \times \Delta\nu, \quad (1)$$

where N_{chan} corresponds to the number of channels across the line width, given by λ_{line}/R , with λ_{line} as the central Bry wavelength, R the KMOS K -band resolution, and $\Delta\nu$ as the channel spacing.

VLA data obtained nearly simultaneously¹ with the KMOS observations were used to investigate temporal correlations between the two. Photometry in the radio images was obtained using the `imfit` task within CASA, which performs Gaussian fitting of the source emission, including error estimation. We take the fitted peak intensity as the source flux. This ensures that the radio flux corresponds to the same arcsecond scale as the KMOS IFU measurement. Also, time-averaged photometry was obtained from the `imfit` results in the concatenated image and from averaging the results in the individual epochs matching the KMOS program (see Section 2.2).

3 RESULTS

3.1 Relationship between Bry and 3.3 cm radio fluxes

Table 1 lists the Bry and radio detections of the YSOs. In the per-epoch images, the radio continuum emission from CrA16 was not detected. However, in the concatenated radio image, this source has a detection at $\approx 94 \pm 21 \mu\text{Jy beam}^{-1}$. The rest of the Bry detected radio sources are detected both in the concatenated image and in individual epochs. Among the YSOs, only JVLA1 and IRS6 have Bry in absorption, whereas in the rest of the detections, the line is in emission. IRS6 is a binary system, and the component designated as IRS6a is the only one with detectable spectral features ([Nisini et al. 2005a](#)).

¹ Since the VLT and VLA epochs were not observed at the exact same time, we consider observations separated by up to ten days as near-simultaneous.

In this paper, references to IRS6 specifically denote the IRS6a component. The Bry absorption line profile of IRS6 is not very wide; hence, we refrain from inferring further about the observed profile. JVLA1 is a class III YSO with a K1 IV subgiant spectral type ([Forbrich & Preibisch 2007](#)). The KMOS spectrum of JVLA1 has prominent absorption features in Bry and the CO (2–0) and (3–1) bandheads. [Sicilia-Aguilar et al. \(2011\)](#) reported minimal infrared excess in JVLA1. Therefore, the absorption lines of JVLA1 likely originate from a cool photosphere.

The time-averaged Bry and 3.3 cm fluxes in our sample are shown in Figure 1. We have used the Bry fluxes averaged over all the observation epochs and the radio fluxes from the concatenated image at 3.3 cm. We have employed a Markov Chain Monte Carlo (MCMC) method for the Bayesian linear regression since it is well suited for datasets containing measurements with uncertainties in both variables. A linear fit to the data gives the following shallow, positive relation:² $\log(F_{3.3 \text{ cm}}) = (4.3 \pm 2.1) + (0.29 \pm 0.12) \times \log(F_{\text{Bry}})$. As we will see in the following, a correlation between these two tracers is not expected for all YSO types.

In the standard scenario of disk evolution, accretion rates are expected to decrease significantly from the class I to the class II YSO stages ([Hartmann et al. 2016](#)). Consequently, if the centimeter free-free emission from YSOs is caused mainly by partially-ionised jets ([Anglada et al. 2018](#)), and if the strength of those jets is linked to that of accretion, a relationship between Bry and radio continuum is expected. This has been recently reported for class II YSOs ([Rota et al. 2024; Garufi et al. 2025](#)), including transition disks ([Rota et al. 2025](#)). However, the faint centimeter continuum from class II YSOs could also be due to disk photo-evaporation by EUV photons ([Pascucci et al. 2014; Galván-Madrid et al. 2014; Macías et al. 2016](#)), which could nevertheless be linked to accretion in a complex way via disk winds ([Pascucci et al. 2023](#)). In the class III stage, where the magnetosphere of the un-embedded young star becomes exposed, centimeter radio emission can become bright again, highly variable, and non-thermal in nature ([Liu et al. 2014; Forbrich et al. 2021](#)). This non-thermal radio emission is not expected to be correlated with accretion phenomena. It is worth mentioning that class 0/I YSOs also exhibit non-thermal radio emission; however, only a few have been observed, e.g., IRS 5 in the Coronet cluster ([Feigelson & Montmerle 1999; Deller et al. 2013; Liu et al. 2014](#)). Such emission is typically identified through circular polarisation, however, it is expected that in the majority of younger YSOs non-thermal emission is easily veiled by the free-free component along the line of sight ([Andre 1987; Deller et al. 2013](#)).

3.2 Relationship between accretion and ionised mass-loss rates

Bry fluxes were converted to the corresponding mass accretion rates (\dot{M}_{acc}) using the relations of [Alcalá et al. \(2017\)](#). Although these relations were calibrated for class II YSOs, we also apply them to class I YSOs, assuming that the underlying accretion engine in class I protostars is similar to that of more evolved class II systems, as supported by recent studies (e.g. [Testi et al. 2025](#)). The stellar parameters of mass (M_*), radius (R_*), and extinction (A_V) are summarised in Table 1. The conversion was carried out for five class I and II sources with Bry detections and for three of the seven upper-limit YSOs with available photometry from VISIONS and *Spitzer*/WISE. The Bry

² Throughout the rest of this paper, radio continuum fluxes are in units of millijansky (mJy), and Bry fluxes are in units of $\text{erg s}^{-1} \text{cm}^{-2}$.

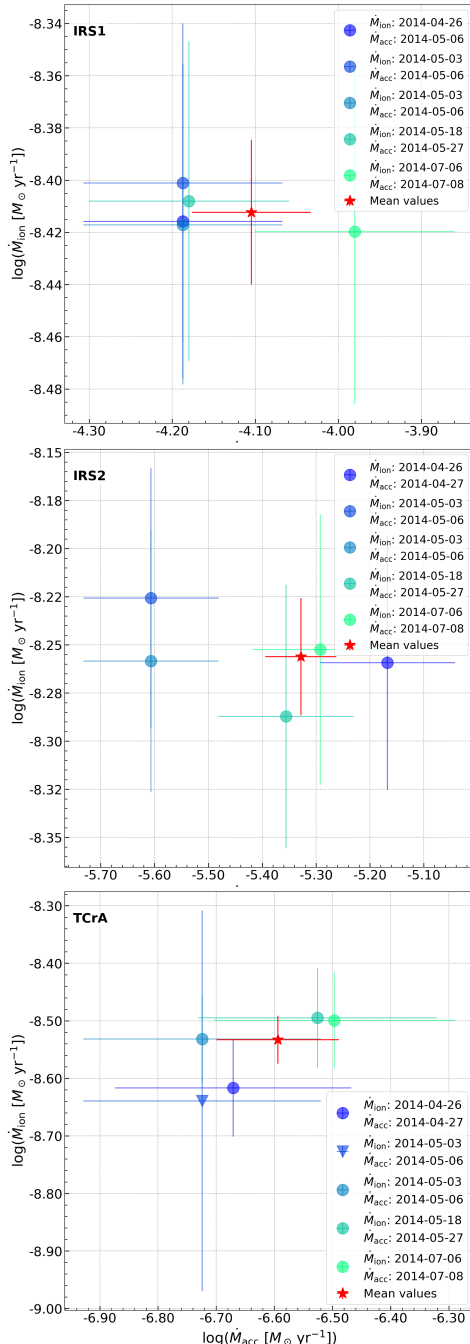


Figure 2. Temporal evolution of individual measurements of \dot{M}_{acc} and \dot{M}_{ion} for the two class I (IRS1, IRS2, top and middle panels) and one class II YSO (TCrA, bottom) with Bry in emission and VLA detection in individual epochs. CrA43 was excluded due to its unphysically large ejection rate compared to its accretion rate (see Section 4.3). The blue and green points refer to values around the individual epochs marked in the plot legends, whereas the red star is the mean value.

fluxes of the YSOs have been extinction corrected with corresponding A_V values using the relation given in Alcalá et al. (2017) and uncertainties in the fluxes, stellar masses, and radii were propagated into the accretion-rate estimates. Since class I YSOs have significant

veiling³ in their spectra, we have followed the recipe described by Fiorellino et al. (2021) to correct for this veiling in our three class I sources; accretion rates were computed over the allowed range of veiling values and combined to derive weighted mean \dot{M}_{acc} estimates.

The 3.3 cm radio continuum fluxes are transformed to ionised mass-loss rates (\dot{M}_{ion}) for the eight class I and II YSOs with an accretion rate measurement or upper limit (see Table 1 in the online supplementary material). Five of them are VLA detections (IRS1, IRS2, CrA43, TCrA, CrA16). For CrA26, Peterson 1, and Peterson 6 we use 3σ from the local noise in the VLA image. The class III YSO JVLA1 has been excluded because the jet interpretation is not appropriate for the radio continuum of the more evolved YSOs (see Section 3.1). We follow equation (11) of Anglada et al. (2018), assuming a conical jet geometry. Disk inclination angles (i) for IRS1, IRS2, TCrA, CrA16, and CrA43 are obtained from Cazzoletti et al. (2019); Hsieh et al. (2024). For sources lacking inclination information, we assume $i = 60^\circ$, corresponding to the median inclination angle expected for a randomly oriented sample. Following Rota et al. (2024), we assume the jet to be perpendicular to the disk plane and therefore aligned with the inclination of the outer disk. The jet velocity (v_{jet}) is estimated from the stellar mass M_* using Equation (12) of Anglada et al. (2018). We conduct this analysis for both the epoch-averaged data and the individual epoch detections. The errors in the mass rates were estimated using the uncertainties⁴ Python package, propagating from the errors in the measured fluxes, disk inclination, jet angular size, jet velocity and electron temperature.

Figure 2 presents the temporal evolution of \dot{M}_{acc} and \dot{M}_{ion} for the three YSOs with individual-epoch measurements. CrA43, although detected in individual epochs, is excluded from further analysis because its derived \dot{M}_{ion} is unphysically larger than \dot{M}_{acc} (see Section 4.3). The three analysed objects, IRS1, IRS2, and TCrA, exhibit variability of 0.12, 0.27, and 0.17 dex, respectively, from their mean rates. No apparent correlation in time is seen between these two quantities, suggesting that a larger temporal coverage is needed (e.g., Takami et al. 2020).

For the time-averaged values, we performed Bayesian linear regression fits to the logarithm of \dot{M}_{ion} as a function of the logarithm of \dot{M}_{acc} under two conditions: *i*) taking the Bry fluxes from the fits to the averaged spectra and the 3.3 cm fluxes from the epoch-concatenated VLA image (see Fig 1 and Fig 2 of the online supplementary material) and *ii*) from averaging the \dot{M}_{acc} and \dot{M}_{ion} values of the near-simultaneous epochs, as shown in Fig. 2, but taking the 3.3 cm flux of CrA16 from the concatenated image and the upper limit fluxes of Peterson 1, Peterson 6, and CrA26 from the concatenated centimeter image and Bry spectra. Based on the expected physical connection between \dot{M}_{ion} and \dot{M}_{acc} , we assume flat bounded priors on the slope (0-2) and intercept (-10 to 10). Figure 3 shows the \dot{M}_{acc} and \dot{M}_{ion} values and fits for these two cases. We also converted the 3.3 cm fluxes at lower angular resolution reported in Liu et al. (2014) into the corresponding \dot{M}_{ion} , and overplotted them in Figure 3, using accretion rates from Nisini et al. (2005a).

The obtained fits to our data are $\log(\dot{M}_{\text{ion}}) = (-7.1 \pm 0.8) + (0.26 \pm 0.13) \times \log(\dot{M}_{\text{acc}})$ for case *i*, and $\log(\dot{M}_{\text{ion}}) = (-7.1 \pm 0.8) + (0.27 \pm 0.14) \times \log(\dot{M}_{\text{acc}})$ for case *ii*. This analysis aimed to assess the impact of temporal variability in our coordinated observations, as YSOs can display short timescale behaviour (e.g. dipper or burster variabil-

³ Veiling refers to the excess continuum emission arising from the circumbinary disk due to the accretion process (e.g., Calvet & Gullbring 1998).

⁴ <https://pypi.org/project/uncertainties/>

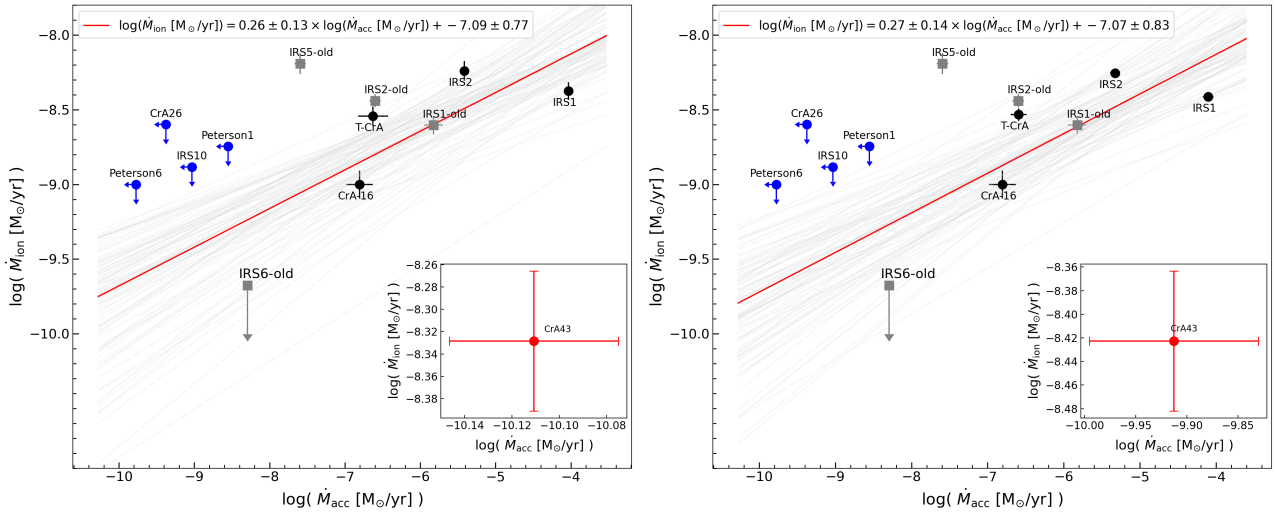


Figure 3. Correlation between the logarithm of the mass accretion rate and the logarithm of the ionised mass-loss rate, including the data from IRS1, IRS2, CrA16, TCrA, Peterson 1, Peterson 6, and CrA 26, but excluding CrA43 (inset) from the fit. We present two fitting scenarios: in the left panel the fit is obtained utilizing the averaged Bry spectra and epoch-concatenated VLA image; in the right panel the fit is obtained from averaging the near-simultaneous measurements shown in Fig. 2 for the detections, and upper limits as described in the text. The light grey lines show regression relations drawn from posterior samples restricted to the central 68% credible interval of the slope; the red line indicates the posterior median. The overplotted gray squares, marked with the suffix “-old”, show previous measurements obtained from Liu et al. (2014) and Nisini et al. (2005a).

ity) capable of significantly affecting the inferred relationships. The observed variations in \dot{M}_{ion} and \dot{M}_{acc} across the monitoring epochs were modest of the order of ~ 0.1 dex, and do not affect the resulting slope of the relation.

4 DISCUSSION

4.1 Ionised ejection with respect to accretion

Figure 4 shows an anti-correlation between the logarithmic ratio $\dot{M}_{\text{ion}}/\dot{M}_{\text{acc}}$ as a function of the logarithm of \dot{M}_{acc} . A linear fit gives $\log(\dot{M}_{\text{ion}}/\dot{M}_{\text{acc}}) = (-7.6 \pm 1.7) - (0.84 \pm 0.29) \times \log(\dot{M}_{\text{acc}})$.

Considering that $\dot{M}_{\text{ejection}}/\dot{M}_{\text{acc}}$ probes the efficiency ξ of the ejection process compared to that accreted by the protostar, in our case, the free-free emission is only sensitive to the ionised component of the ejected material, ξ_{ion} , not to the neutral atomic (Nisini et al. 2018) or molecular (Ray et al. 2023) components. The ξ_{ion} values in our sample are consistent with those reported by Rota et al. (2024, 2025), who also used the free-free continuum for a sample of class II YSOs mostly located in the Taurus star formation region. Our ξ_{ion} values are also consistent with those of Nisini et al. (2018). However, their ejection rates were derived from the high velocity component of the [O i] line in a sample of 131 class II YSOs in several star forming regions. Rota et al. (2025) showed that, although full discs (FDs) typically accrete at higher rates than transition discs (TDs), the accretion-wind scaling is shallower in TDs, implying a reduced apparent efficiency. The four sources for which we could perform the full analysis are two class IIs and, for the first time, two class I YSOs.

Several reports of rings and gaps in class I disks have been presented (e.g., Sheehan et al. 2020; Hsieh et al. 2024), but the details of mass transport in the disks of embedded YSOs are far from understood. In class II YSOs, studies on magneto-centrifugal launching models have shown that ξ is inversely proportional to the magnetic lever arm λ^{-1} (Pelletier & Pudritz 1992; Hartmann et al. 2016; Pasucci et al. 2023). This implies that lower ξ values correspond to larger λ , thus resulting in more compact jet launching regions. The

lower ξ_{ion} values for class I YSOs in our sample may therefore point to narrower launching zones or different magnetic field morphologies, a scenario pointed out by Nisini et al. (2018).

On the other hand, protostellar jets are known to have a nested structure, consisting of high-velocity ionised winds enclosed by layers of atomic and molecular jets with decreasing velocity gradients (e.g., Nisini et al. 2024; Bacciotti et al. 2025). Therefore, another possible interpretation of the trend shown in Fig. 4 considers the chemical and ionization state of the ejected material, which can be either atomic ionised, atomic neutral, or molecular.⁵ A full account of the efficiency of ejected to accreted material should consider these three states, i.e., $\xi_{\text{tot}} = \xi_{\text{ion}} + \xi_{\text{ato}} + \xi_{\text{mol}}$ (e.g., Fedriani et al. 2019). Assuming that ξ_{tot} remains constant across YSO evolutionary stages, the observed decrease in ξ_{ion} with evolutionary stage suggests that jets are predominantly neutral (atomic and molecular) in the earlier protostellar phases, with the ionization fraction increasing as the YSOs evolve. This scenario is supported by previous studies of Herbig-Haro objects HH 34 (Nisini et al. 2016) and HH 211 (Ray et al. 2023).

4.2 Accretion and ejection variability

Regarding the short-term (days to months) time evolution shown in Fig. 2, there is no clear evidence of a temporal correlation between accretion and ionised mass-loss rates. This can be understood by considering the timescale of the formation of lobes of ionised gas in the jet, which we approximate as $\sim 0.5 \times \text{beamsize} / \text{jet velocity}$, or $\sim 10^2$ days. Connelley & Greene (2014) reported the variability of near-IR tracers of accretion and winds in a sample of class I YSOs with a four year survey. They concluded that both types of tracers are sometimes positively or negatively correlated and sometimes uncorrelated, depending on the target. Similar results were obtained by Ellerbroek et al. (2014) in the Herbig Ae/Be star

⁵ For simplicity, we neglect the contribution of ionised molecular species.

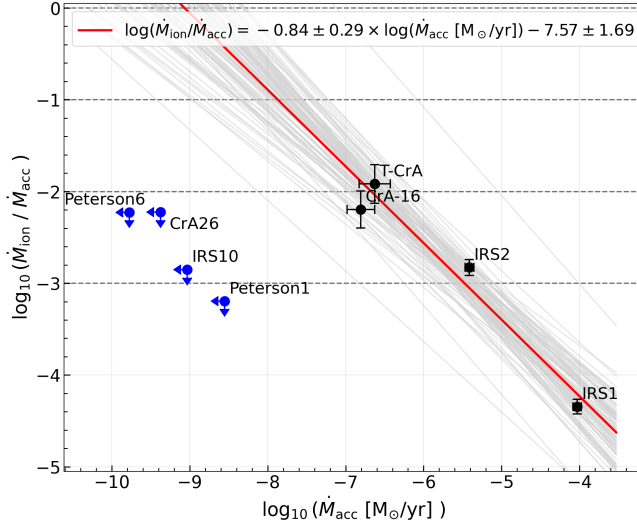


Figure 4. Logarithm of the ratio of the ionised mass-loss rate to the mass-accretion rate, as a function of the latter. The horizontal lines mark efficiency factors $\xi_{\text{ion}} = 0.001, 0.01, 0.1$, and 1 . The red and grey lines are defined as in Fig. 2.

HD 163296 and by Forbrich et al. (2015) in LRLL 54361. Also, the class 0 YSO HOPS 383, which presented a $\times 35$ increment in bolometric luminosity between 2004 and 2006 (Safron et al. 2015), did not present a corresponding increase in the centimetre flux of the associated radio jet (Galván-Madrid et al. 2015). All these results highlight the complexity of the physical relationship between accretion and ejection in jets and winds (see e.g., Romanova et al. 2018; Zhu 2025, for detailed simulations). The observed variability in accretion and ionised mass-loss rates in Fig. 2 is probably due to the inherent stochasticity in these processes (Fischer et al. 2023).

4.3 Outliers and complex behaviour

The class I YSO CrA43 was excluded from further analysis due to its inferred \dot{M}_{ion} being two orders of magnitude larger than the corresponding \dot{M}_{acc} (see inset plot of Fig. 3). We consider the possible explanation for this anomaly. The KMOS observations were taken during a state of quiescence. During such an episode of a lower accretion rate, the radio jet core could also become optically thin, allowing non-thermal radio emission from the magnetosphere, if present, to reach the observer (e.g., Liu et al. 2014). More generally, variability in both accretion (e.g., Costigan et al. 2014; Claes et al. 2022) and jet ejection (e.g., Reipurth et al. 2002; Takami et al. 2023) could be an important source of the observed scatter and outliers in studies like the one presented in this paper, even if we attempted to perform observations as simultaneously as possible.

5 CONCLUSIONS

Using multi-epoch coordinated observations with KMOS-VLT and the VLA, we have measured the Bry line and 3.3 cm radio continuum emission for 26 YSOs in the Coronet Cluster. Accretion and ionised jet ejection rates were derived from both tracers for 4 YSOs with confirmed detections, while upper limits were obtained for an additional 4 YSOs. Using time-averaged measurements, we find a sub-linear relation between \dot{M}_{acc} and \dot{M}_{ion} , with a slope of $\approx 0.3 \pm 0.1$ in logarithmic space. This implies that the amount of ionised jet ejection

follows that of mass accretion across the protostar to protoplanetary disk evolutionary timescales of up to a few Myr. However, we do not find a clear relationship between these quantities in our time monitoring sampling timescales from days to months, possibly due to the complex interplay between magnetospheric accretion and jet launching processes.

DATA AVAILABILITY

The data underlying this article are available in its online supplementary material.

ACKNOWLEDGEMENTS

Based on observations collected at the European Organisation for Astronomical Research in the Southern Hemisphere under ESO programme 093.C-0657. The National Radio Astronomy Observatory is a facility of the National Science Foundation operated under co-operative agreement by Associated Universities, Inc. A.G., R.G.M., J.R.A., and C.C.G. acknowledge support from CONAHCyT Ciencia de Frontera project ID 86372 “Cítlalcoatl”. These authors also thank the support from DGAPA-UNAM and UNAM-PAPIIT projects IN105225 and IG101224. R.G.M. acknowledges support from the ESO Scientific Visitor Programme. H.B.L. is supported by the National Science and Technology Council (NSTC) of Taiwan (Grant Nos. 111-2112-M-110-022-MY3, 113-2112-M-110-022-MY3). The authors thank Stefan Meingast for providing VISIONS photometric data. This research has made use of the following software: **Astropy** (Astropy Collaboration et al. 2018, 2022), and **CASA** (CASA Team et al. 2022).

References

- Adams F. C., Lada C. J., Shu F. H., 1987, *ApJ*, **312**, 788
- Alcalá J. M., et al., 2017, *A&A*, **600**, A20
- Andre P., 1987, in Montmerle T., Bertout C., eds, Protostars and Molecular Clouds. p. 143
- Andre P., Ward-Thompson D., Barsony M., 1993, *ApJ*, **406**, 122
- Anglada G., Rodríguez L. F., Carrasco-González C., 2018, *A&ARv*, **26**, 3
- Armitage P. J., Clarke C. J., Palla F., 2003, *MNRAS*, **342**, 1139
- Astropy Collaboration et al., 2018, *AJ*, **156**, 123
- Astropy Collaboration et al., 2022, *ApJ*, **935**, 167
- Bacciotti F., et al., 2025, *arXiv e-prints*, p. arXiv:2501.03920
- Banzatti A., Pascucci I., Edwards S., Fang M., Gorti U., Flock M., 2019, *ApJ*, **870**, 76
- CASA Team et al., 2022, *PASP*, **134**, 114501
- Calvet N., Gullbring E., 1998, *ApJ*, **509**, 802
- Cazzoletti P., et al., 2019, *A&A*, **626**, A11
- Choi M., Hamaguchi K., Lee J.-E., Tatematsu K., 2008, *ApJ*, **687**, 406
- Claes R. A. B., et al., 2022, *A&A*, **664**, L7
- Connelley M. S., Greene T. P., 2014, *AJ*, **147**, 125
- Contreras Peña C., et al., 2017, *MNRAS*, **465**, 3039
- Costigan G., Vink J. S., Scholz A., Ray T., Testi L., 2014, *MNRAS*, **440**, 3444
- Davies R. I., et al., 2013, *A&A*, **558**, A56
- Deller A. T., Forbrich J., Loinard L., 2013, *A&A*, **552**, A51
- Dong R., Najita J. R., Brittain S., 2018, *ApJ*, **862**, 103
- Dunham M. M., et al., 2014, in Beuther H., Klessen R. S., Dullemond C. P., Henning T., eds, Protostars and Planets VI. pp 195–218 ([arXiv:1401.1809](https://arxiv.org/abs/1401.1809)), doi:10.2458/azu_uapress_9780816531240-ch009
- Dzib S. A., Loinard L., Ortiz-León G. N., Rodríguez L. F., Galli P. A. B., 2018, *ApJ*, **867**, 151
- Ellerbroek L. E., et al., 2014, *A&A*, **563**, A87

Fang M., et al., 2018, [ApJ](#), **868**, 28

Fedriani R., et al., 2019, [Nature Communications](#), **10**, 3630

Feigelson E. D., Montmerle T., 1999, [ARA&A](#), **37**, 363

Fiorellino E., et al., 2021, [A&A](#), **650**, A43

Fischer W. J., Hillenbrand L. A., Herczeg G. J., Johnstone D., Kospal A., Dunham M. M., 2023, in Inutsuka S., Aikawa Y., Muto T., Tomida K., Tamura M., eds, Astronomical Society of the Pacific Conference Series Vol. 534, Protostars and Planets VII. p. 355 ([arXiv:2203.11257](#)), doi:10.48550/arXiv.2203.11257

Folha D. F. M., Emerson J. P., 2001, [A&A](#), **365**, 90

Forbrich J., Preibisch T., 2007, [A&A](#), **475**, 959

Forbrich J., et al., 2007, [A&A](#), **464**, 1003

Forbrich J., Rodríguez L. F., Palau A., Zapata L. A., Muzerolle J., Gutermuth R. A., 2015, [ApJ](#), **814**, 15

Forbrich J., Dzib S. A., Reid M. J., Menten K. M., 2021, [ApJ](#), **906**, 23

Frank A., et al., 2014, in Beuther H., Klessen R. S., Dullemond C. P., Henning T., eds, Protostars and Planets VI. pp 451–474 ([arXiv:1402.3553](#)), doi:10.2458/azu_uapress_9780816531240-ch020

Freudling W., Romaniello M., Bramich D. M., Ballester P., Forchi V., García-Dabló C. E., Moehler S., Neeser M. J., 2013, [A&A](#), **559**, A96

Gaidos E., Gehrig L., Güdel M., 2025, [A&A](#), **696**, A207

Galli P. A. B., Bouy H., Olivares J., Miret-Roig N., Sarro L. M., Barrado D., Berihuete A., Brandner W., 2020, [A&A](#), **634**, A98

Galván-Madrid R., et al., 2014, [A&A](#), **570**, L9

Galván-Madrid R., Rodríguez L. F., Liu H. B., Costigan G., Palau A., Zapata L. A., Loinard L., 2015, [ApJ](#), **806**, L32

Garufi A., et al., 2025, [A&A](#), **694**, A290

Guo Z., et al., 2020, [MNRAS](#), **492**, 294

Hartigan P., Edwards S., Ghadour L., 1995, [ApJ](#), **452**, 736

Hartmann L., Herczeg G., Calvet N., 2016, [ARA&A](#), **54**, 135

Hsieh C.-H., Arce H. G., Maureira M. J., Pineda J. E., Segura-Cox D., Mardones D., Dunham M. M., Arun A., 2024, [ApJ](#), **973**, 138

Liu H. B., et al., 2014, [ApJ](#), **780**, 155

Lora V., Nony T., Esquivel A., Galván-Madrid R., 2024, [ApJ](#), **962**, 66

Macías E., et al., 2016, [ApJ](#), **829**, 1

Manara C. F., AnsdeLL M., Rosotti G. P., Hughes A. M., Armitage P. J., Lodato G., Williams J. P., 2023, in Inutsuka S., Aikawa Y., Muto T., Tomida K., Tamura M., eds, Astronomical Society of the Pacific Conference Series Vol. 534, Protostars and Planets VII. p. 539 ([arXiv:2203.09930](#)), doi:10.48550/arXiv.2203.09930

Meingast S., et al., 2023, [A&A](#), **673**, A58

Miettinen O., Kontinen S., Harju J., Higdon J. L., 2008, [A&A](#), **486**, 799

Morales-Calderón M., et al., 2011, [ApJ](#), **733**, 50

Muzerolle J., Calvet N., Hartmann L., 2001, [ApJ](#), **550**, 944

Myers P. C., 2009, [ApJ](#), **700**, 1609

Nisini B., Antoniucci S., Giannini T., Lorenzetti D., 2005a, [A&A](#), **429**, 543

Nisini B., Antoniucci S., Giannini T., Lorenzetti D., 2005b, [A&A](#), **429**, 543

Nisini B., Giannini T., Antoniucci S., Alcalá J. M., Bacciotti F., Podio L., 2016, [A&A](#), **595**, A76

Nisini B., Antoniucci S., Alcalá J. M., Giannini T., Manara C. F., Natta A., Fedele D., Biazzo K., 2018, [A&A](#), **609**, A87

Nisini B., et al., 2024, [ApJ](#), **967**, 168

Pascucci I., Ricci L., Gorti U., Hollenbach D., Handler N. P., Brooks K. J., Contreras Y., 2014, [ApJ](#), **795**, 1

Pascucci I., Cabrit S., Edwards S., Gorti U., Gressel O., Suzuki T. K., 2023, in Inutsuka S., Aikawa Y., Muto T., Tomida K., Tamura M., eds, Astronomical Society of the Pacific Conference Series Vol. 534, Protostars and Planets VII. p. 567 ([arXiv:2203.10068](#)), doi:10.48550/arXiv.2203.10068

Pelletier G., Pudritz R. E., 1992, [ApJ](#), **394**, 117

Peterson D. E., et al., 2011, [ApJS](#), **194**, 43

Pudritz R. E., Ouyed R., Fendt C., Brandenburg A., 2007, in Reipurth B., Jewitt D., Keil K., eds, Protostars and Planets V. p. 277 ([arXiv:astro-ph/0603592](#)), doi:10.48550/arXiv.astro-ph/0603592

Ray T. P., et al., 2023, [Nature](#), **622**, 48

Reipurth B., Rodríguez L. F., Anglada G., Bally J., 2002, [AJ](#), **124**, 1045

Robitaille T. P., Whitney B. A., Indebetouw R., Wood K., 2007, [ApJS](#), **169**, 328

Rodríguez L. F., Zapata L. A., Dzib S. A., Ortiz-León G. N., Loinard L., Macías E., Anglada G., 2014, [ApJ](#), **793**, L21

Romanova M. M., Blinova A. A., Ustyugova G. V., Koldoba A. V., Lovelace R. V. E., 2018, [New Astron.](#), **62**, 94

Rota A. A., Meijerhof J. D., van der Marel N., Francis L., van der Tak F. F. S., Sellek A. D., 2024, [A&A](#), **684**, A134

Rota A. A., et al., 2025, [arXiv e-prints](#), p. arXiv:2505.16586

Safron E. J., et al., 2015, [ApJ](#), **800**, L5

Sharples R., et al., 2013, [The Messenger](#), **151**, 21

Sheehan P. D., Tobin J. J., Federman S., Megeath S. T., Looney L. W., 2020, [ApJ](#), **902**, 141

Shu F., Najita J., Ostriker E., Wilkin F., Ruden S., Lizano S., 1994, [ApJ](#), **429**, 781

Sicilia-Aguilar A., Henning T., Juhász A., Bouwman J., Garmire G., Garmire A., 2008, [ApJ](#), **687**, 1145

Sicilia-Aguilar A., Henning T., Kainulainen J., Roccatagliata V., 2011, [ApJ](#), **736**, 137

Skrutskie M. F., et al., 2006, [AJ](#), **131**, 1163

Takami M., et al., 2006, [ApJ](#), **641**, 357

Takami M., et al., 2020, [ApJ](#), **901**, 24

Takami M., et al., 2023, [ApJS](#), **264**, 1

Testi L., et al., 2025, [A&A](#), **703**, A277

Tychoniec L., et al., 2018, [ApJS](#), **238**, 19

Williams J. P., Cieza L. A., 2011, [ARA&A](#), **49**, 67

Zhu Z., 2025, [MNRAS](#), **537**, 3701

SUPPLEMENTARY MATERIAL

Figure 1 shows the VLT-KMOS detections of the Bry line listed in Table 1, and Figure 2 shows the corresponding 3.3 cm radio continuum emission.

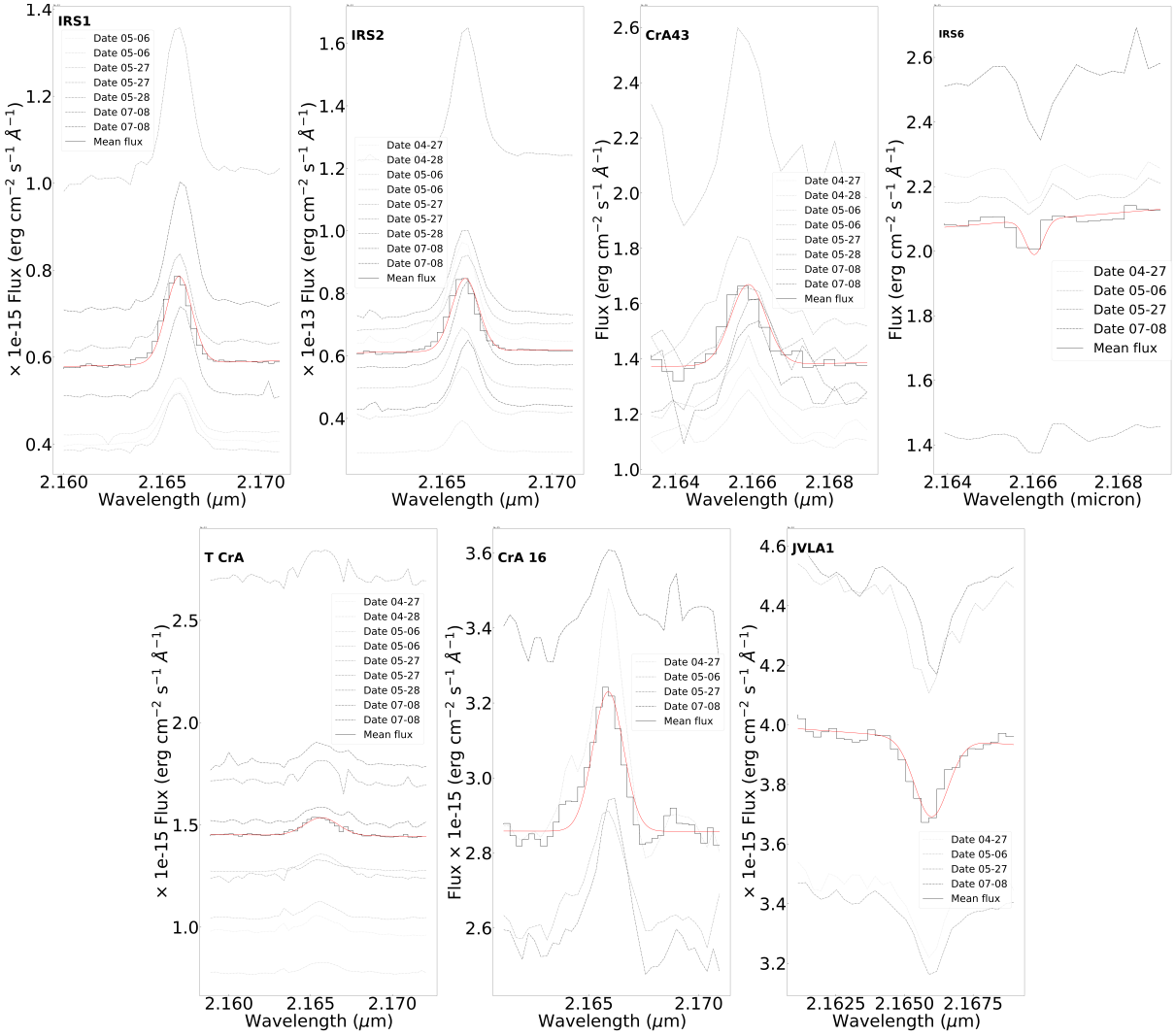


Figure 1. Bry line profiles of the seven YSOs with a detection listed in Table 1. The broken grey lines show the spectra in individual epochs, whereas the step plot in black shows their average. The red line represents the Gaussian fit to the mean spectrum.

This paper has been typeset from a $\text{\TeX}/\text{\LaTeX}$ file prepared by the author.

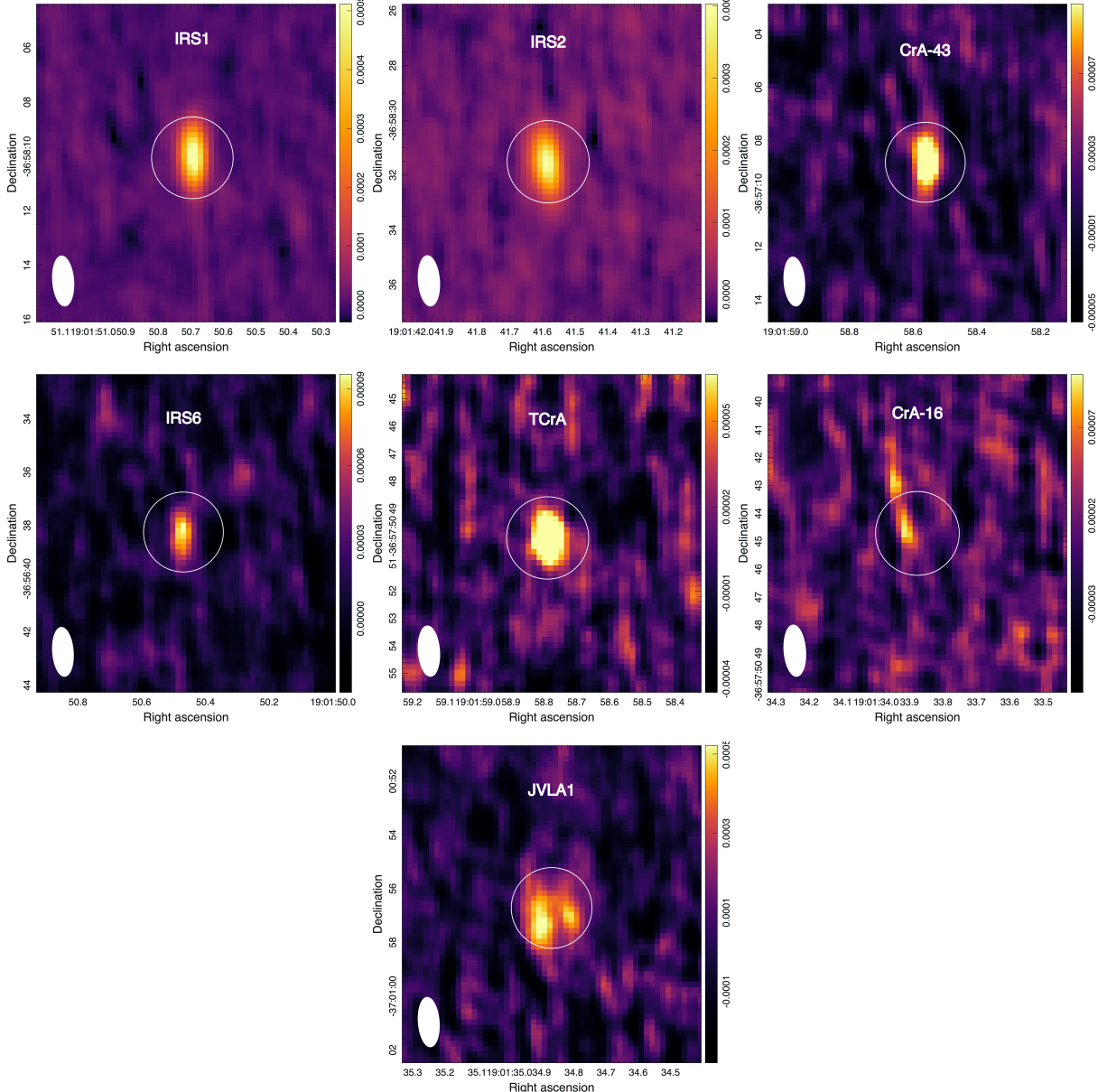


Figure 2. 3.3 cm radio-continuum emission from the seven YSOs in the Coronet with $\text{Br}\gamma$ detection. The marker circles are centered at the coordinates listed in Table 1. The color scale is normalized to the minimum and maximum intensities within each panel, using a square root color stretch.

Table 2. Bry and 3.3 cm radio continuum fluxes for the YSOs listed in Table 2. Columns from left to right are: source name, observation dates, per-epoch Bry flux, per-epoch 3.3 cm flux, Bry flux from averaged spectrum, and 3.3 cm flux from concatenated-data image. The fluxes marked with \dagger are upper limits.

Source	Date	F_{Bry} [erg s $^{-1}$ cm $^{-2}$]	$F_{3.3\text{cm}}$ [mJy]	$\overline{F_{\text{Bry}}}$ [erg s $^{-1}$ cm $^{-2}$]	$\overline{F_{3.3\text{cm}}}$ [mJy]
IRS1	03-17		0.499 ± 0.019		
	04-22		0.706 ± 0.019		
	04-26		0.496 ± 0.011		
	05-03		0.519 ± 0.019		
	05-06	$2.16\text{e-}17 \pm 3.19\text{e-}19$			
	05-06	$2.31\text{e-}17 \pm 7.33\text{e-}19$			
	05-18		0.508 ± 0.020	$3.34\text{e-}17 \pm 6.48\text{e-}19$	0.563 ± 0.009
	05-27	$5.69\text{e-}17 \pm 1.64\text{e-}18$			
	07-06		0.490 ± 0.042		
	07-08	$3.22\text{e-}17 \pm 9.91\text{e-}19$			
IRS2	07-11		0.994 ± 0.039		
	08-09		0.530 ± 0.016		
	09-01		0.519 ± 0.026		
	03-17		0.371 ± 0.022		
	04-22		0.303 ± 0.068		
	04-26		0.377 ± 0.012		
	04-27	$4.99\text{e-}17 \pm 1.21\text{e-}18$			
	05-03		0.418 ± 0.022		
	05-06	$2.86\text{e-}17 \pm 6.38\text{e-}19$		$3.55\text{e-}17 \pm 6.81\text{e-}19$	0.399 ± 0.013
	05-18		0.346 ± 0.022		
CrA16	05-27	$3.47\text{e-}17 \pm 8.32\text{e-}19$			
	07-06		0.385 ± 0.031		
	07-08	$3.92\text{e-}17 \pm 7.45\text{e-}19$			
	07-11		0.681 ± 0.104		
	08-09		0.490 ± 0.040		
CrA26 Peterson 1 Peterson 6 Peterson 7 CrA9 IRS10 Haas17	09-01		0.590 ± 0.021		
	04-27	$1.02\text{e-}18 \pm 9.52\text{e-}20$		$6.45\text{e-}19 \pm 5.40\text{e-}20$	0.094 ± 0.021
	05-06	$5.84\text{e-}19 \pm 5.56\text{e-}20$			
	05-27	$6.46\text{e-}19 \pm 5.58\text{e-}20$			
	07-08	$3.49\text{e-}19 \pm 7.81\text{e-}20$			
				$1.03\text{e-}20^\dagger$	0.061^\dagger
				$2.45\text{e-}20^\dagger$	0.087^\dagger
				$1.03\text{e-}21^\dagger$	0.078^\dagger
				$6.29\text{e-}21^\dagger$	0.054^\dagger
				$7.37\text{e-}21^\dagger$	0.165^\dagger
				$7.68\text{e-}21^\dagger$	0.084^\dagger
				$4.53\text{e-}21^\dagger$	0.072^\dagger